Supplementary Information

Synergistic Diameter Control and Post-Treatment Engineering of Electrospun PVDF Nanofibers toward β-Phase Enrichment and Enhanced Piezoelectric Response

Han Qiu[1], Yang Xiao[1], Mohong Xu[1], Yiming Zhang[1], Hezhi He[1,*], Zhiwen Zhu[1,*]

[1] *National Engineering Research Center of Novel Equipment for Polymer Processing, Laboratory of Polymer Processing Engineering of Ministry of Education, Guangdong Provincial Key Laboratory of Technique and Equipment for Macromolecular Advance Manufacturing, South China University of Technology, Guangzhou 510641, P. R. China*

* Corresponding authors. Emails: pmhzhe@scut.edu.cn (H. He) and mrobito@163.com (Z. Zhu)

Table of Content

Supplementary Note 1. Influence of Molecular Weight on Chain Entanglement and Rearrangement during Electrospinning

During the electrospinning process, polymer solutions exhibit a critical entanglement concentration (C*), which corresponds to the onset of sufficient intermolecular chain entanglements required for stable jet formation. Near this concentration, polymer solutions generally display optimal spinnability and enable the fabrication of continuous fibers with well-defined morphologies. Based on polymer physics, the entanglement concentration can be estimated as:

$$C^* = \frac{K}{M^{\beta}(1+\alpha)^{\gamma}} \tag{1-1}$$

Where C∗ is the entanglement concentration of the spinning solution, expressed in units of g/mL or mol/L; M is the average molecular weight of the polymer; α represents the molecular weight distribution breadth, commonly characterized by the polydispersity index (PDI = Mw/Mn), with Mw and Mn denoting the weight-average and number-average molecular weights, respectively; and K, β, and γ are empirical constants related to the specific polymer system. According to this relationship, polymer solutions with higher molecular weights and broader molecular weight distributions exhibit lower critical entanglement concentrations, allowing effective chain entanglement to be achieved at reduced polymer concentrations.

In this work, spinning solutions were prepared by blending a small fraction of high-molecular-weight PVDF (Mw = 670,000 g mol^{-1}) with low-molecular-weight PVDF (Mw = 180,000 g mol^{-1}), resulting in a broadened molecular weight distribution. This strategy enables sufficient chain entanglement at relatively low solution concentrations, thereby facilitating electrospinning in the ultrafine fiber regime. The electrospinning performance of PVDF solutions with different molecular weight ratios was systematically investigated. As shown in Figure S1, solutions with low total polymer content (1–3%, 1–4%, and 1–5%) exhibit extensive bead formation and fiber breakage, indicating insufficient chain entanglement and an unstable jet. Increasing the solution composition to 2–3% significantly improves fiber continuity, although occasional breakage remains. At a ratio of 2–5%, uniform nanofibers with smooth

surfaces and a narrow diameter distribution are obtained, with an average fiber diameter of approximately 108 nm.

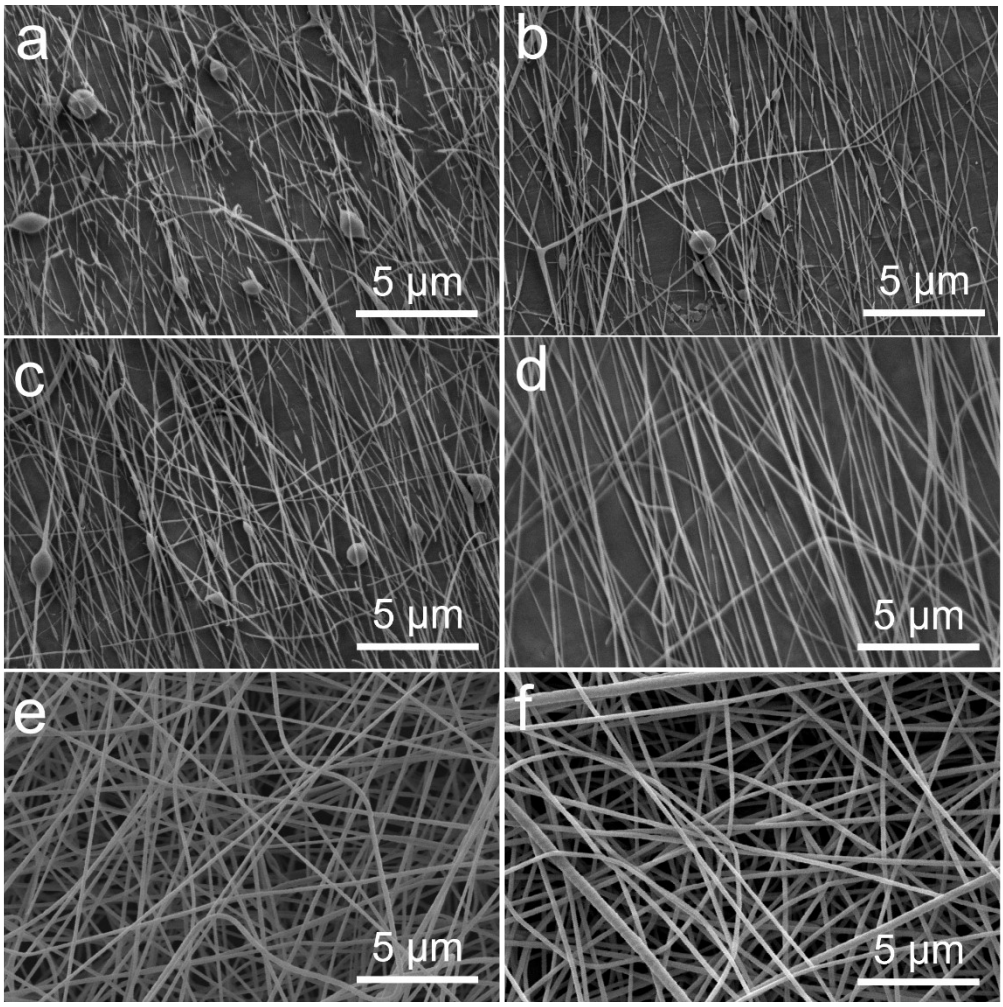

Figure S1. SEM images of PVDF fibers prepared from mixed molecular weight PVDF solutions at different concentrations: (a) 1-3%; (b) 1-4%; (c) 1-5%; (d) 2-3%; (e) 2-5%; (f) 2-7%.

To further elucidate the role of molecular weight, electrospinning experiments were also conducted using single-component high-molecular-weight PVDF solutions (Mw = 670,000 g mol^{-1}) at concentrations ranging from 2% to 9% (Figure S2). At low concentrations (2–3%), severe bead formation and fiber discontinuity are observed, reflecting insufficient entanglement density and excessive jet stretching under the electric field. As the concentration increases to 4–5%, a stable entanglement network is established, leading to continuous fibers with improved morphology. Further increases in concentration (≥7%) markedly raise solution viscosity and entanglement density, thereby limiting jet stretching and resulting in progressively thicker fibers.

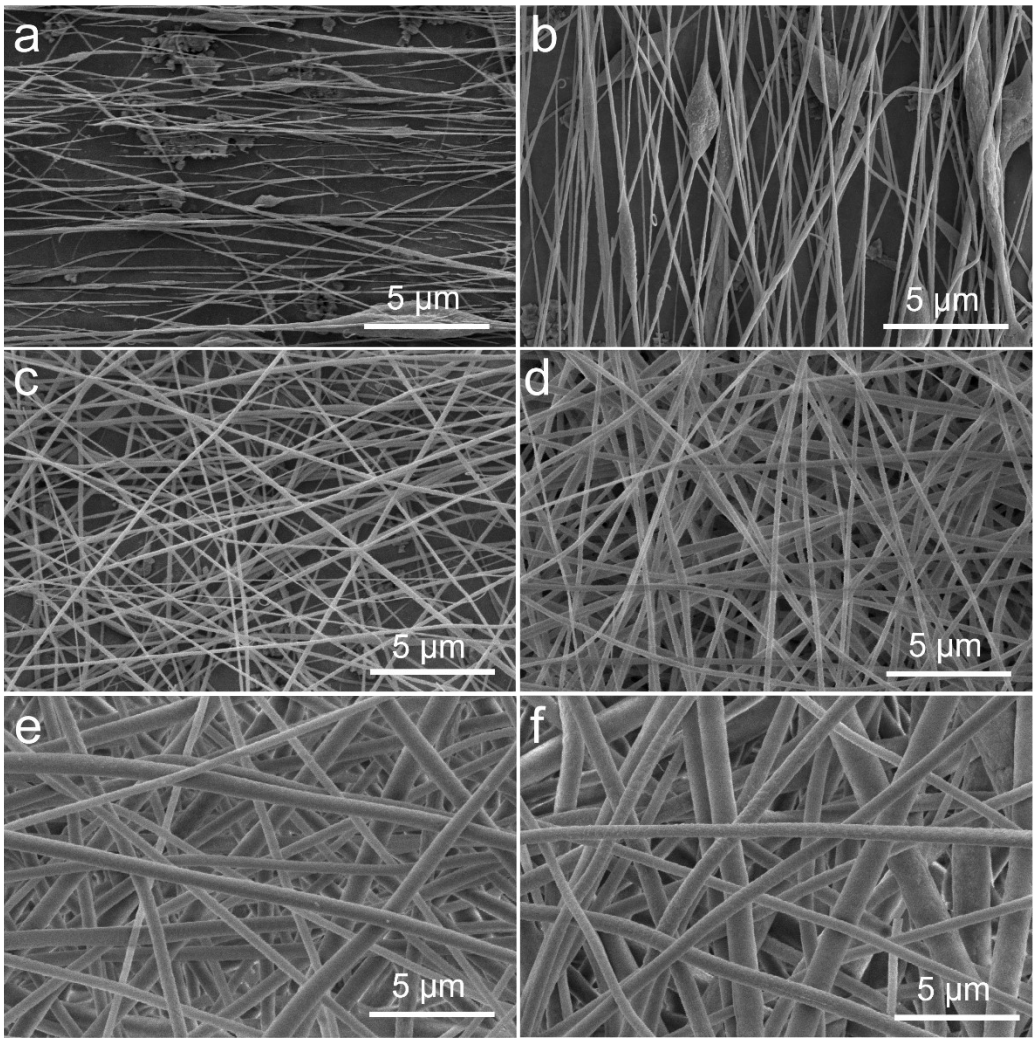

Figure S2. SEM images of fibers prepared from PVDF solutions (Mw=670,000 $g mol^{-1}$) at different concentrations: (a) 2%; (b) 3%; (c) 4%; (d) 5%; (e) 7%; (f) 9%.

From a molecular perspective, PVDF solutions containing a higher fraction of high-molecular-weight chains form more strongly entangled networks, which impose greater constraints on jet elongation and slow down chain rearrangement during stretching and solidification. In contrast, solutions enriched with low-molecular-weight PVDF possess looser entanglement networks, allowing more extensive jet stretching and more rapid chain orientation along the fiber axis. Importantly, these molecular-weight-dependent effects primarily manifest as variations in fiber diameter and diameter distribution, which are explicitly characterized and systematically controlled in this study.

Therefore, although variations in molecular weight influence chain entanglement and rearrangement dynamics during electrospinning, their effects are intrinsically incorporated into the resulting fiber morphology—particularly fiber diameter. Since the

piezoelectric performance is analyzed as a function of fiber diameter over a representative range (0.1–1.0 μm), the influence of molecular weight does not introduce an uncontrolled bias but is instead implicitly accounted for through the controlled variation of this key structural parameter.

In summary, the combined investigation of mixed and single molecular weight PVDF solutions establishes a well-defined electrospinning window for producing PVDF nanofibers with uniform morphology and tunable diameters. This framework provides a consistent basis for correlating molecular characteristics, fiber structure, and piezoelectric performance.

Table 1. Average fiber diameters of fibers electrospun from PVDF solutions at different concentrations.

PVDF Concentration (%)	Average Diameter (nm)	PVDF Concentration (%)	Average Diameter (nm)
2	/	1-3	/
3	/	1-4	/
4	/	1-5	/
5	240	2-3	/
7	490	2-5	109
9	900	2-7	250

Supplementary Note 2. Schematic diagram of a bias controlled grid corona poling setup

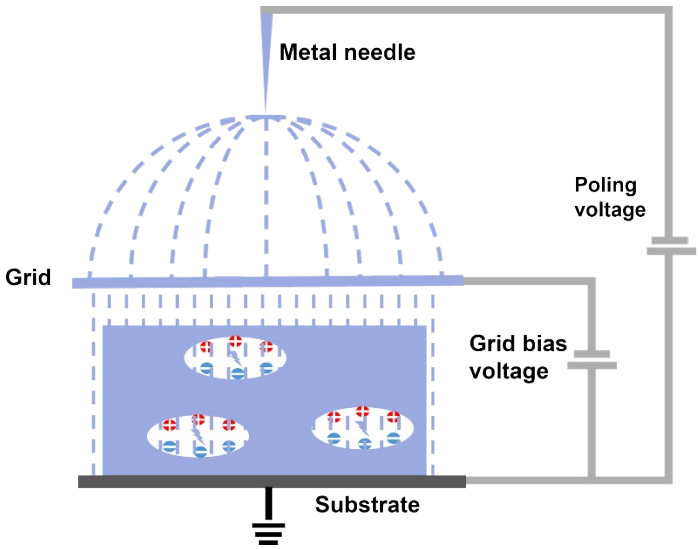

Figure S3. Setup of the corona poling system.

Supplementary Note 3. Crystal structure of PVDF nanofibers with different diameters

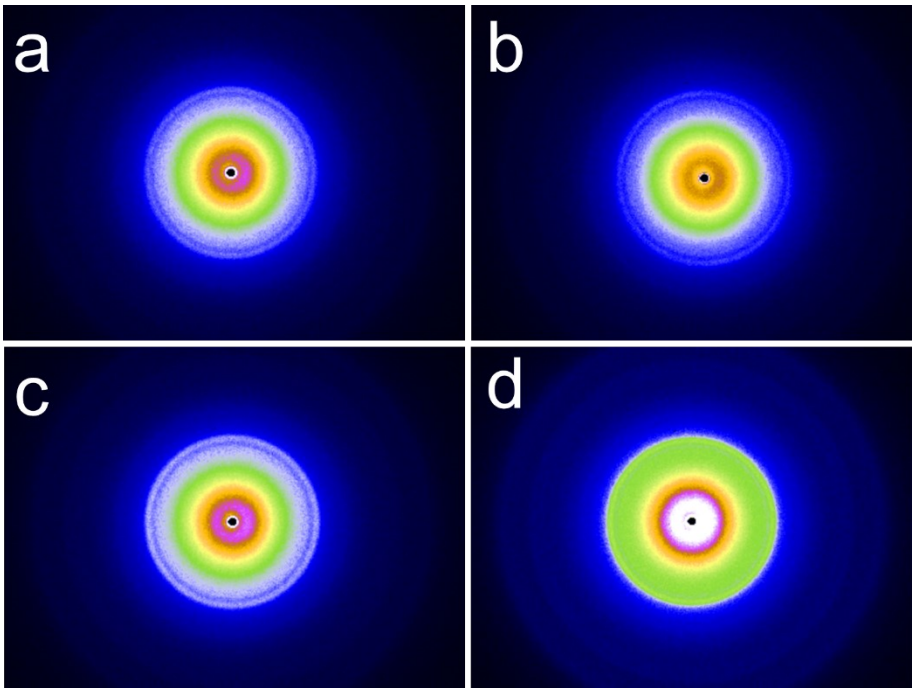

Figure S4. 2D wide-angle X-ray diffraction (2D WAXD) patterns of PVDF nanofibers with different diameters obtained from solutions: (a) ES-2-5%; (b) ES-5%; (c) ES-7%; (d) ES-9%.

Supplementary Note 4. A switching-polarity study

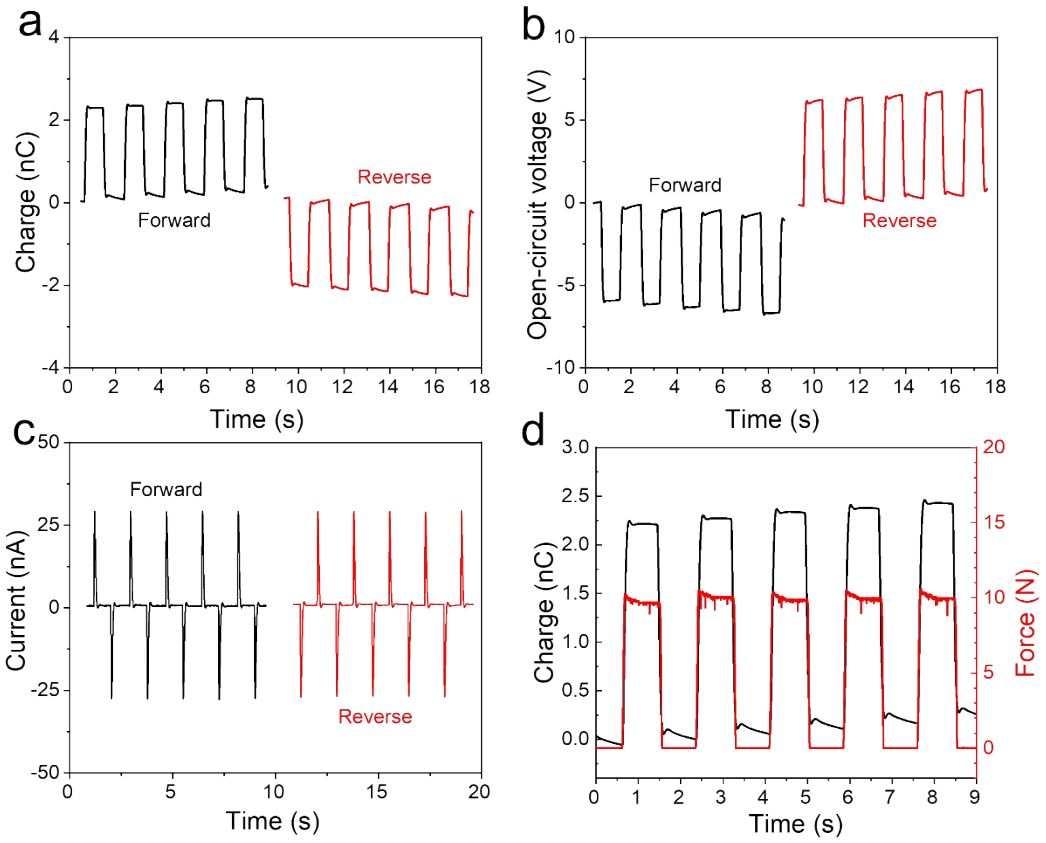

Figure S5. Output performance of ES-2-5% PVDF piezoelectric devices under a cyclic compressive force of 10.3 N with forward and reverse electrical connections: (a) piezoelectric charge output; (b) open-circuit voltage; (c) short-circuit current output; (d) piezoelectric charge output and applied force curve.

Supplementary Note 5. Verification of the induced dipole effect under corona poling

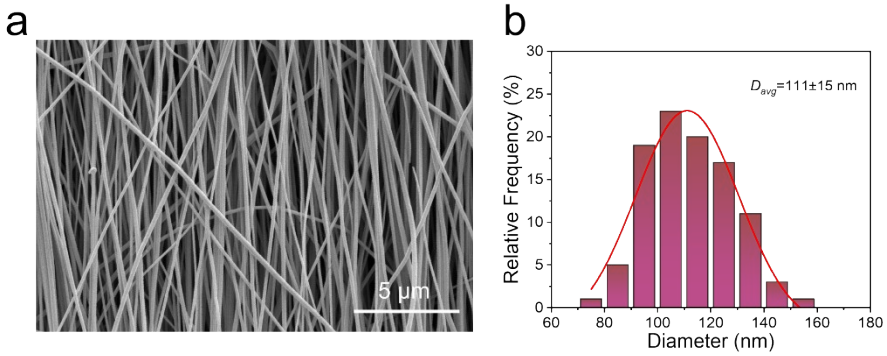

Figure S6. SEM morphology and fiber-diameter distribution of the PVA nanofiber membrane.

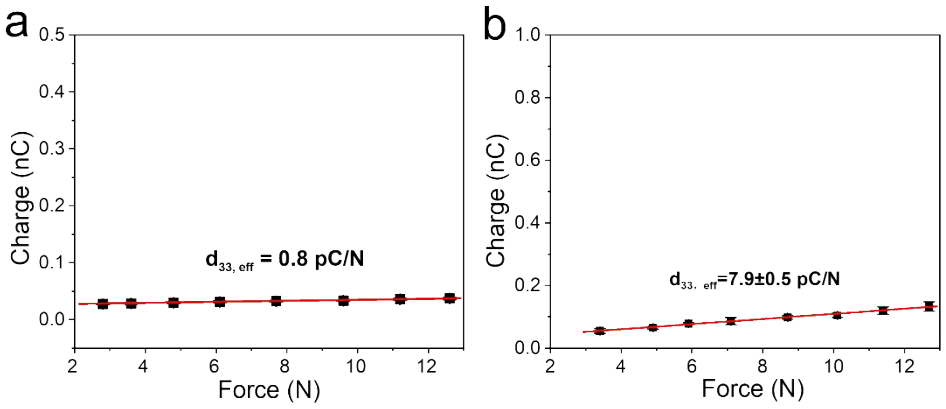

Figure S7. Force–charge curves and effective piezoelectric coefficient of the PVA nanofiber membrane before and after poling: (a) unpoled; (b) poled for 30 min.

Supplementary Note 6. Piezoelectric performance of nopole ES-2-5% PVDF nanofiber mats

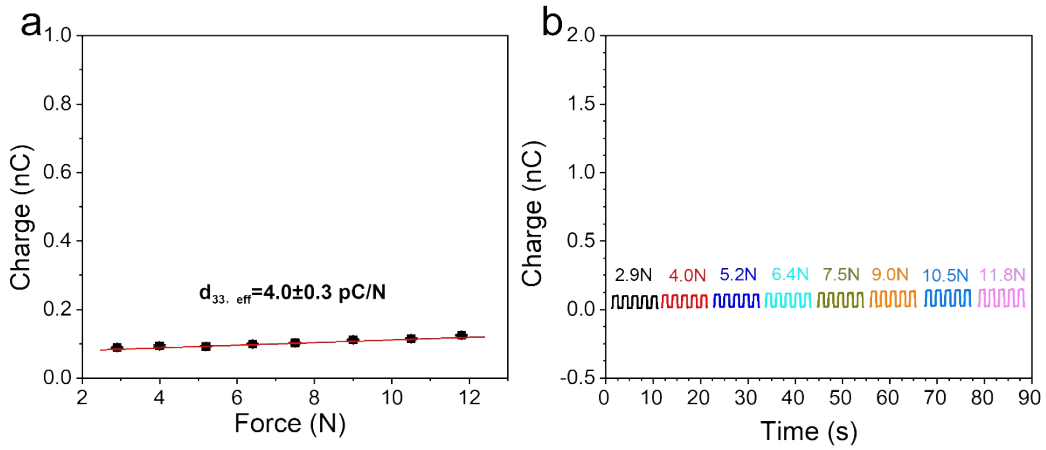

Figure S8. Piezoelectric performance of unpolarized ES-2-5% PVDF nanofiber membranes: (a) linear fit of piezoelectric charge versus cyclic compressive forces ranging from 2.9 N to 11.8 N; based on the slope, the piezoelectric coefficient was calculated as 4.0 pC N^{-1}; (b) piezoelectric charge output under cyclic compressive forces of different frequencies.

Supplementary Note 7. Piezoelectric performance of commercial PVDF film

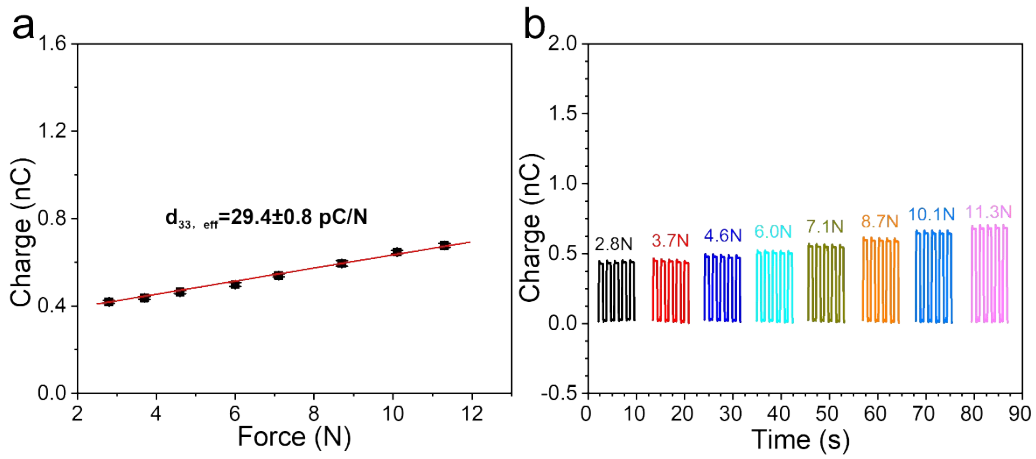

Figure S9. Piezoelectric performance of commercial PVDF film. (a) Linear fit of the piezoelectric charge output of commercial PVDF film with applied periodic compressive force ranging from 2.0 N to 12.0 N. From the slope, the piezoelectric coefficient of commercial PVDF film was calculated to be 29.4 pC N^{-1}. (b) Piezoelectric charge output of commercial PVDF film under different periodic compressive forces.

Supplementary Note 8. Effect of annealing on PVDF nanofiber morphology and properties

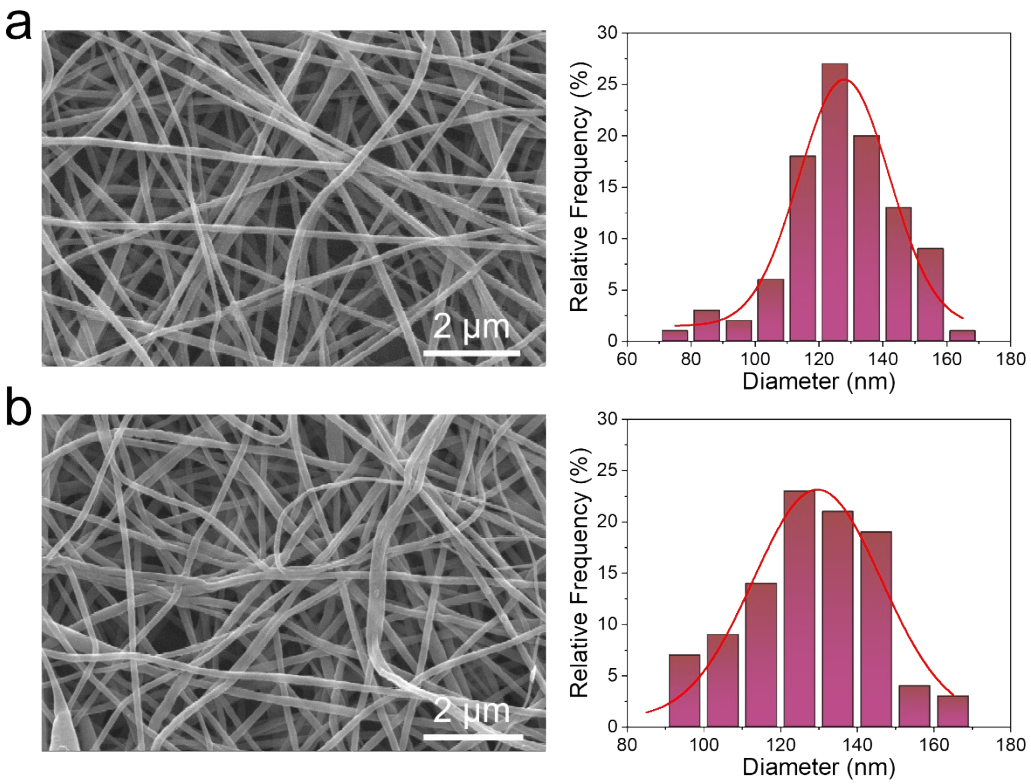

Figure S10. SEM images and diameter distributions of ES-2-5% PVDF nanofibers annealed at different temperatures: (a) morphology and diameter distribution of ES-2-5%-A140°C fibers; (b) morphology and diameter distribution of ES-2-5%-A150°C fibers.

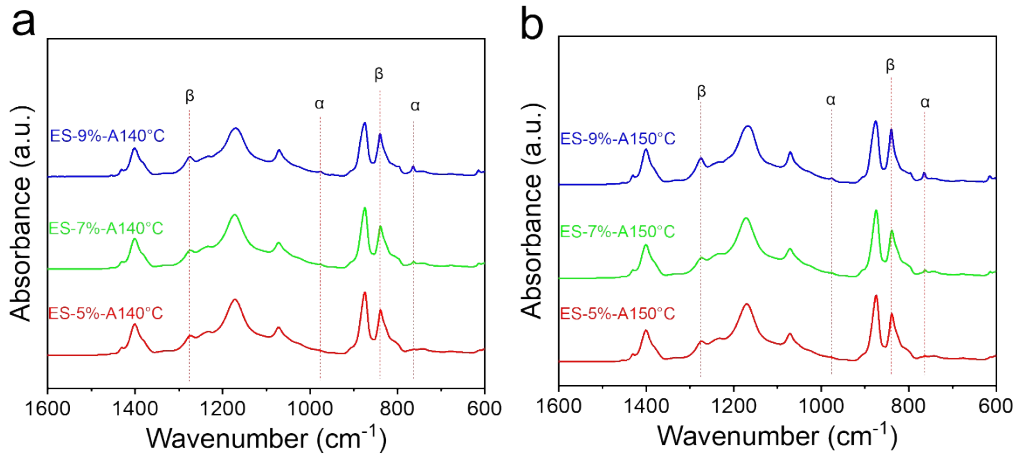

Figure S11. FT-IR spectra of ES-5%, ES-7%, and ES-9% PVDF nanofibers annealed

at 140°C and 150°C for 12 h: (a) FT-IR curves of ES-5%-A140°C, ES-7%-A140°C, and ES-9%-A140°C; (b) FT-IR curves of ES-5%-A150°C, ES-7%-A150°C, and ES-9%-A150°C.

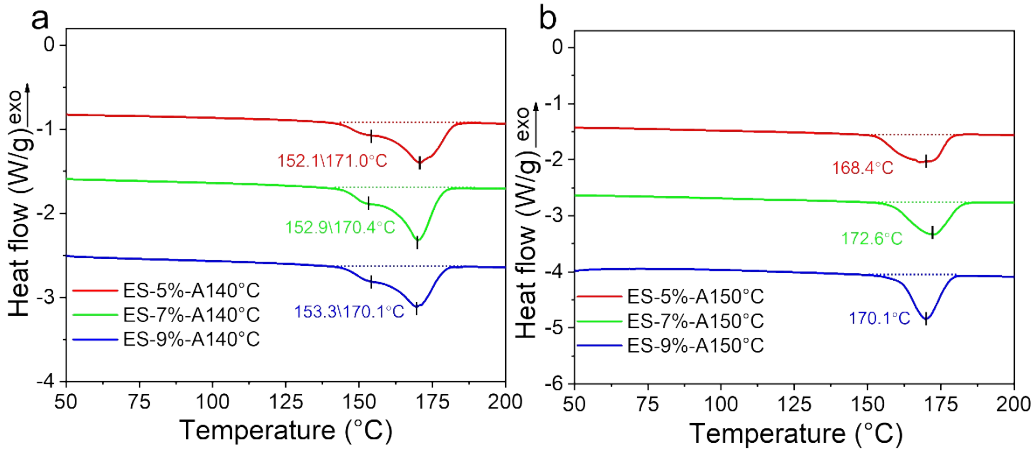

Figure S12. DSC curves of ES-5%, ES-7%, and ES-9% PVDF nanofibers annealed at 140°C and 150°C for 12 h: (a) DSC curves of ES-5%-A140°C, ES-7%-A140°C, and ES-9%-A140°C; (b) DSC curves of ES-5%-A150°C, ES-7%-A150°C, and ES-9%-A150°C.

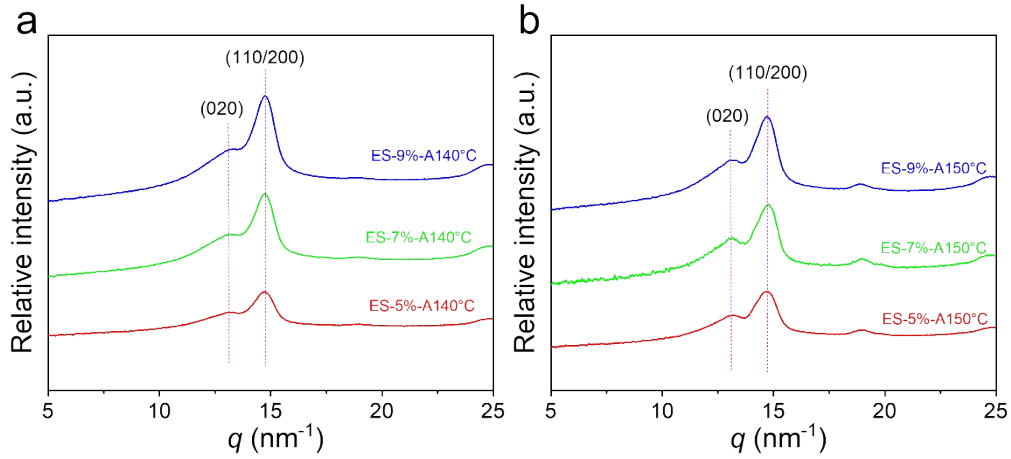

Figure S13. XRD patterns of ES-5%, ES-7%, and ES-9% PVDF nanofibers annealed at 140°C and 150°C for 12 h: (a) XRD patterns of ES-5%-A140°C, ES-7%-A140°C, and ES-9%-A140°C; (b) XRD patterns of ES-5%-A150°C, ES-7%-A150°C, and ES-9%-A150°C.

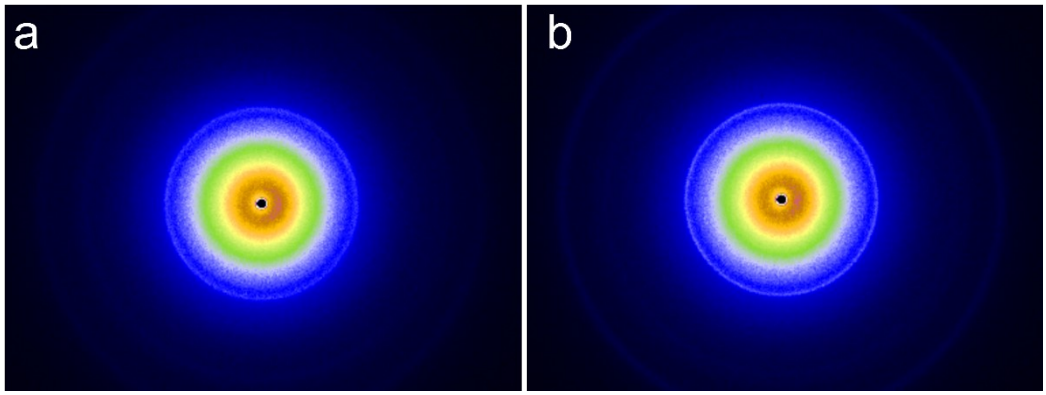

Figure S14. 2D-WAXD images of ES-2-5% PVDF nanofibers annealed at 140°C and 150°C for 12 h: (a) ES-2-5%-A140°C; (b) ES-2-5%-A150°C.

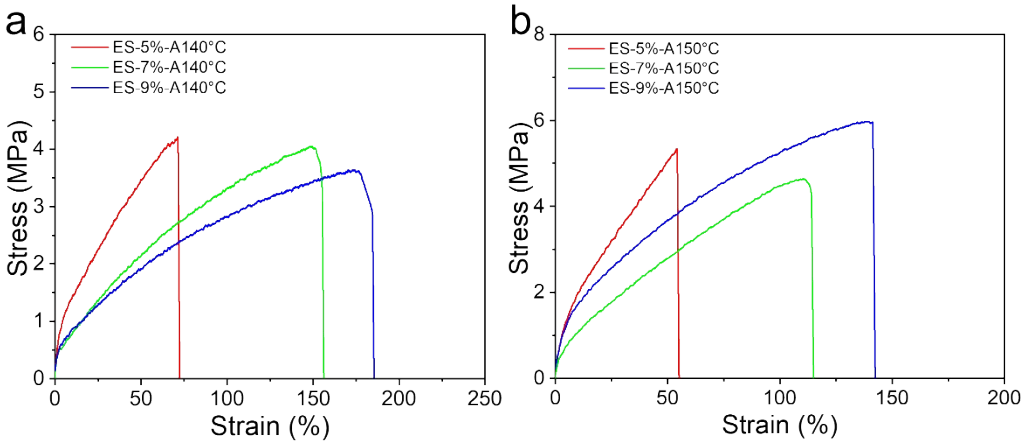

Figure S15. Stress-strain curves of ES-5%, ES-7%, and ES-9% PVDF nanofibers annealed at 140°C and 150°C for 12 h: (a) stress-strain curves of ES-5%-A140°C, ES-7%-A140°C, and ES-9%-A140°C; (b) stress-strain curves of ES-5%-A150°C, ES-7%-A150°C, and ES-9%-A150°C.

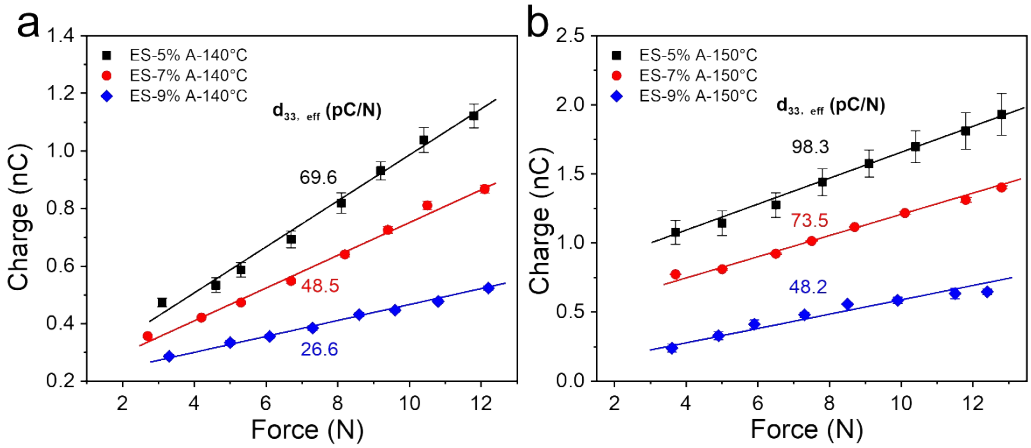

Figure S16. Piezoelectric performance of ES-5%, ES-7%, and ES-9% PVDF nanofibers annealed at 140°C and 150°C for 12 h: (a) linear fitting of piezoelectric charge output versus cyclic compressive forces from 2.0 N to 13.0 N for PVDF nanofiber membranes annealed at 140°C; (b) linear fitting of piezoelectric charge output versus cyclic compressive forces from 2.0 N to 13.0 N for PVDF nanofiber membranes annealed at 150°C.

Supplementary Note 9. Calculation of the effective piezoelectric phase content

Table 2. The content of effective piezo phase (Cep) calculation results of PVDF nanofiber mats

Sample	Xc	F(β)	Content of effective piezo phase (Cep)
ES-2-5%	0.386	0.912	0.3520
ES-5%	0.431	0.821	0.3539
ES-7%	0.432	0.795	0.3434
ES-9%	0.443	0.757	0.3354
ES-2-5% A140°C	0.534	0.934	0.4988
ES-2-5% A150°C	0.541	0.951	0.5145

Xc: crystallinity calculated from the first heating DSC melting curve; F(β): β-phase content calculated from the FT-IR spectrum.

Supplementary Note 10. Comparison of piezoelectric properties and preparation methods

Table 3. Comparison of piezoelectric properties and preparation methods between PVDF nanofiber film and other PVDF based piezoelectric materials reported in literature.

Morphology	Material	Fabrication method	Piezoelectric response	β-phase content	Ref.
Film	PVDF	Biaxially oriented、Unidirectionally poled	-62 pC N^{-1}	100%	1
	PVDF	Folding-hot-pressing	20 pC N^{-1}	97.5%	2
	PVDF	Solvent-assisted	-25.8 pC N^{-1}	98.8%	3
	PVDF/$CaCl_2$	Ionic doping/ Annealing	29.26 pm V^{-1}	92.78%	4
	PVDF/IL	Stretching/Annealing	51.8 pm V^{-1}	/	5
	PVDF/BTO	Self-poled	51.20 pC N^{-1}	/	6
Nanofiber mat	PVDF/CNF@ZnO	Electrospun	31.00±2.07 pC·N^{-1}	86.97%	7
	PVDF/$Al(NO_3)_3$·$9H_2O$	Electrospun	−116 pm V^{-1}	/	8
	PVDF-g-MA/ BT@PDA	Electrospun/ Assembly	76.2 pC N^{-1}	83.7%	9
	PVDF/MXene	Electrospun	61.7 pC N^{-1}	/	10
	PVDF/Chitosan	Electrospun	35 pC·N^{-1}	63.7%	11
	PVDF	Electrospun	−21 pC·N^{-1}	80.25%	12
	PVDF	Electrospun/ Annealing	136.0 pC·N^{-1}	95.1%	This work

Supplemental references

1. Y. Huang, G. Rui, Q. Li, E. Allahyarov, R. Li, M. Fukuto, G.-J. Zhong, J.-Z. Xu, Z.-M. Li, P. L. Taylor and L. Zhu, *Nature Communications*, 2021, **12**, 675.
2. J. Shen, Y. Zeng, Q. Li, J. Zhou and W. Chen, *Interdisciplinary Materials*, 2024, **3**, 715-725.
3. X. Li, Y. Wang, T. He, Q. Hu and Y. Yang, *Journal of Materials Science: Materials in Electronics*, 2019, **30**, 20174-20180.
4. D. Hazarika, J. Lu, J. Wu, M. N. Shah, J. Li, K. Zhang, L. Xu, C. Chen, Z. Cao, H. Jin, S. Dong, Y. Huang, Q. Zhang, Y. Wu and J. Luo, *npj Flexible Electronics*, 2025, **9**, 20.
5. Z. Ye, J. Yi, Y. Zhang and C. Xiong, *Advanced Materials Technologies*, 2025, **10**, 2401447.
6. Z.-X. Huang, L.-W. Li, Y.-Z. Huang, W.-X. Rao, H.-W. Jiang, J. Wang, H.-H. Zhang, H.-Z. He and J.-P. Qu, *Nature Communications*, 2024, **15**, 819.
7. Q. Zhu, X. Song, X. Chen, D. Li, X. Tang, J. Chen and Q. Yuan, *Nano Energy*, 2024, **127**, 109741.
8. Y. M. Yousry, K. Yao, S. Chen, W. H. Liew and S. Ramakrishna, *Advanced Electronic Materials*, 2018, **4**, 1700562.
9. D. Cui, J. Wang, M. Zhang, T. Cheng, N. Yue, D. Qiu, B. Lu, B. Dong, C. Shen and C. Liu, *Advanced Functional Materials*, 2024, **34**, 2404503.
10. L. Jin, Y. Ao, T. Xu, J. Zhang, Y. Zou, B. Lan, S. Wang, W. Deng and W. Yang, *Journal of Materials Chemistry A*, 2025, **13**, 14446-14454.
11. S. Zhou, H. Zhang, C. Du, M. Liu, L. Liu and Y. Zhang, *ACS Applied Electronic Materials*, 2024, **6**, 2575-2583.
12. A. S. Zahari, M. H. Mazwir and I. I. Misnon, *Polimery*, 2021, **66**, 532-537.